Proximity effects in superconducting spin-valve structures

Flokstra, M.G.

Chapter 6

Probing reversed proximity in the spin-valve using LE-μSR

6.1 Introduction

The main characteristics of the (superconducting) proximity effect of the S/F interface are the emergence of spin triplet correlations and the oscillatory nature of the induced order parameter in F. For these interfaces, the key parameters of S are the superconducting gap energy Δ and the superconducting coherence length ξ_S, while in F they are the exchange energy $E_{\rm ex}$ (of the exchange field $H_{\rm ex}$) and coherence length ξ_F. For thin film, where we usually are in the dirty limit, the layer thicknesses become important as well and the following relations apply: $\xi_S = \sqrt{\hbar D_S/\Delta}$ and $\xi_F = \sqrt{\hbar D_F/E_{\rm ex}}$, where D_S and D_F are the diffusion constants of the S and F layer respectively. While usually the focus is on the leaking of Δ (superconducting correlations) in F, the inverse process occurs as well, which is the leaking of $E_{\rm ex}$ (ferromagnetic correlations) in S. This would lead to a certain amount of magnetization in the S layer. Calculations performed recently indicate that this can be a measurable effect [31]. However, the commonly used measurement techniques, such as transport measurements or surface probing, are unsuited for detecting the reversed proximity effect, at least, in the way they are conventionally applied. The mechanism of the reversed proximity essentially is a form of spin polarization, or actually a spin dependent suppression, of the Cooper pairs near the S/F interface. For the Cooper pairs which have an electron impinging the F layer, the pair breaking strength experienced is lowest if the electron spin is aligned with the exchange field. The result is that more (a higher density) of these aligned Cooper pairs remain compared to the other orientations. This (partial) alignment of the Cooper pair is in real space and when the electron with parallel spin direction is near the interface, the other electron of the Cooper pair (which has an anti-parallel spin direction) is roughly at a distance ξ_S from the interface. In the situation where the parallel electron is mainly located on the F side of the interface, the S side of the interface will have a higher density of anti-parallel electrons, while in the situation that the parallel electron is still mainly on the S side, the net spin polarization oscillates from parallel (near the interface) to anti-parallel (at roughly ξ_S from the interface), and back to neutrality (at roughly few times ξ_S away from the interface). This mechanism is shown in Fig. 6.1.

To investigate this (possible) induced magnetism in the superconductor we need a measurement technique that can locally probe the magnetic moments in the superconductor near the F/S interface, "near" meaning down to the scale of ξ_S, which is about 10 nm in our devices. Low energy muon spin rotation

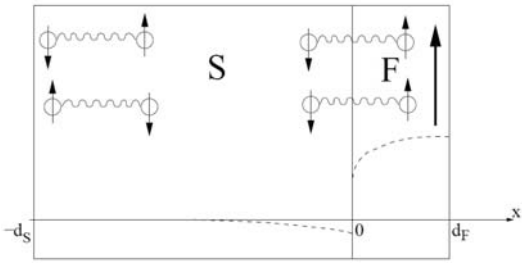

Figure 6.1: Schematic of the inverse proximity resulting in polarized Cooper pairs. The dashed lines indicate the field profile. Figure taken from [31].

(LE-μSR) is one such technique, other are e.g. the (optical) Kerr effect, and Nuclear Magnetic Resonance, and both these techniques have recently been used to investigate the inverse proximity effect [71, 72]. We come back to this in the discussion. LE-μSR makes use of spin polarized muons, which act as local magnetic field probes when implanted into a sample. The implantation (or stopping) profile depends on the muon energy and becomes broader for higher energies. Low energy muons mean energies in the keV range, which allows for probing down to the nanometer scale. All our LE-μSR measurements were done at the Paul Scherrer Institut (PSI) in Villigen (Switzerland) in collaboration with S. Lee and co-workers from St.Andrews University (Scotland). The LE-μSR technique is a rather recent development, developed at PSI in early 2000 (see [73] for a review on this). A nice demonstration of this technique on related spin-valve samples are the experiments conducted on Fe/Ag/Fe [74] and Fe/Pb/Fe [75] thin films. The first experiment revealed the existence of a spin density wave across the normal metallic Ag spacer layer. The second experiment showed that such spin density wave still exists when the spacer layer becomes superconducting (Pb has a bulk superconducting transition temperature of 7.2 K). These spin density waves stretch across the full spacer layer making it ideal for LE-μSR. The spin density wave is also a manifestation of spin polarization but now from the conduction electrons. Two important differences between a spin density wave and the inverse proximity effect are the length over which the effect takes place, and the number of oscillation they produce in the spin polarization profile. The spin density wave easily covers the full S layer thickness while making multiple oscillations (order of 10), while the inverse proximity effect is focussed near the interfaces and makes a half to a full oscillation.

low energy muon spin resonance and low energy muon-spin relaxation are also commonly used for this abbreviation

6.2 Description of the measurement technique

In this section we first introduce the principle of the muon spin rotation technique, and then give a detailed description of the working of the experimental setup.

6.2.1 Principle of muon spin rotation

The essential principle of the muon spin rotation technique comes down to be able to follow the time evolution of a single muon spin. In the presence of a local magnetic field (B), the muon starts to precess around this field (Lamor precession) with a frequency (ω_μ) given by:

$$\omega_\mu = \gamma_\mu B \tag{6.1}$$

where $\gamma_\mu = 851$ MHz T^{-1} is the gyromagnetic ratio for the muon. When the muon decays it emits a positron at an angle θ with respect to the momentary muon spin direction (which is the most preferred direction). The probability distribution for this angle is given by:

$$W(\theta) = 1 + \frac{1}{3}\cos(\theta) \tag{6.2}$$

which is an energy averaged value of the positron spectrum. By detecting the emitted positron, (a fraction of) information is recovered about the muon spin at the moment of the decay. When placed between two positron counter detectors, the value of the magnetic field (B) can be recovered by making a large number of single muon measurements (events), by simply counting the positrons and record the time span of each event. Two main prerequisites are that each event should be about identical in the starting situation (such that the results can be added) and the muon has to be detected before entering the sample to start the measurement timer. Thus, a monochromatic spin-polarized muon beam is essential for the experiment. Fig. 6.2 shows a simplified schematic of the muon spin rotation setup. The initial muon spin direction at $t = t_0 = 0$ is pointing towards the left positron counter detector and the corresponding angle is ϕ_0, with a anticlockwise precession direction of frequency ω_μ. At a certain time $t > t_0$, the muon spin has rotated over an angle $\omega_\mu t$ and the muon spin direction has become $\phi(t) = \omega_\mu t + \phi_0$. The chance that the muon decays at that instance is given by $(1/\tau_\mu)e^{-t/\tau_\mu}$, with τ_μ the muon lifetime. Throughout this chapter we use the convention that t_0 signals the moment that the actual precession starts with ϕ_0 being the starting angle of the muon spin, measured with respect to the muon spin pointing towards the left detector (in the figure this implies $\phi_0 = 0$). Furthermore, the starting time is set to zero, $t_0 \equiv 0$. The detectors do not cover all possible angles, leaving a range of angles for which the emitted positron will not be detected,

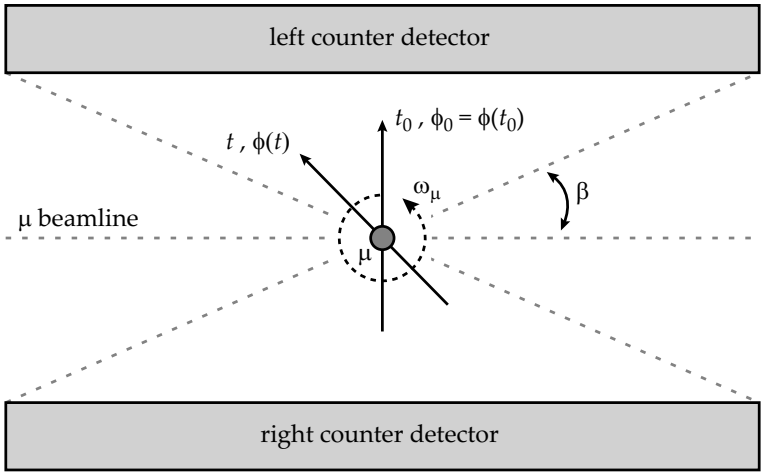

Figure 6.2: Basic setup of the muon spin rotation experiment. Here t_0 and ϕ_0 are the initial time and starting angle of the muon (μ) spin. At time $t > t_0$ the spin direction has rotated anticlockwise with frequency ω_μ and has now angle ϕ.

this "dark-angle" is parameterized by β. To calculate the probability that at t a positron is detected on the left (right) detector we need to integrate the positron emission angle probability function $W(\theta)$ over all values of theta that cause the positron to arrive at the left (right) detector, and multiply by the chance that the muon actually decayed at that time. These probabilities are given by:

$$\begin{aligned}
P_{\mathrm{L}}(t) &= \tfrac{1}{2\pi\tau_\mu} e^{-\frac{t}{\tau_\mu}} \int_{\theta=\theta_1}^{\theta_2} \left(1 + \tfrac{1}{3}\cos(\theta)\right) d\theta = \tfrac{\beta'}{\tau_\mu}\left(1 + A_0(t)\right) e^{-\frac{t}{\tau_\mu}} \\
P_{\mathrm{R}}(t) &= \tfrac{1}{2\pi\tau_\mu} e^{-\frac{t}{\tau_\mu}} \int_{\theta=\theta_1+\pi}^{\theta_2+\pi} \left(1 + \tfrac{1}{3}\cos(\theta)\right) d\theta = \tfrac{\beta'}{\tau_\mu}\left(1 - A_0(t)\right) e^{-\frac{t}{\tau_\mu}} \\
A_0(t) &= \tfrac{P_{\mathrm{L}}(t) - P_{\mathrm{R}}(t)}{P_{\mathrm{L}}(t) + P_{\mathrm{R}}(t)} = -\tfrac{1}{3}\tfrac{\sin\left(\phi(t) - \pi\beta'\right) - \sin\left(\phi(t) + \pi\beta'\right)}{2\pi\beta'} \\
\theta_1 &= -\phi(t) + \beta - \pi/2 \;,\; \theta_2 = -\phi(t) - \beta + \pi/2 \\
\beta' &\equiv \tfrac{\pi - 2\beta}{2\pi} \;,\; \phi(t) = \omega_\mu t + \phi_0 = \gamma_\mu B t + \phi_0
\end{aligned} \tag{6.3}$$

Here, the pre-factor $1/(2\pi)$ is to normalize the probability function $W(\theta)$ and β' is the angular fractional covering of a detector plate. Furthermore, $A_0(t)$ is the so-called asymmetry signal which weighs the difference between counted event on the left and right detector. It contains all physical information about the muon precession, and thus the magnetic structure, and plays an important role in the data analysis. In the limit of full covering detector plates ($\beta \to 0$) the asymmetry value has a maximum of ± 0.21, while in the limit of point detectors ($\beta \to \pi/2$) it has a maximum value of ± 0.33. Although the asymmetry is improved for a point-like detector, the counts per second on the detector

will be much decreased. Model detector signals and asymmetry are plotted

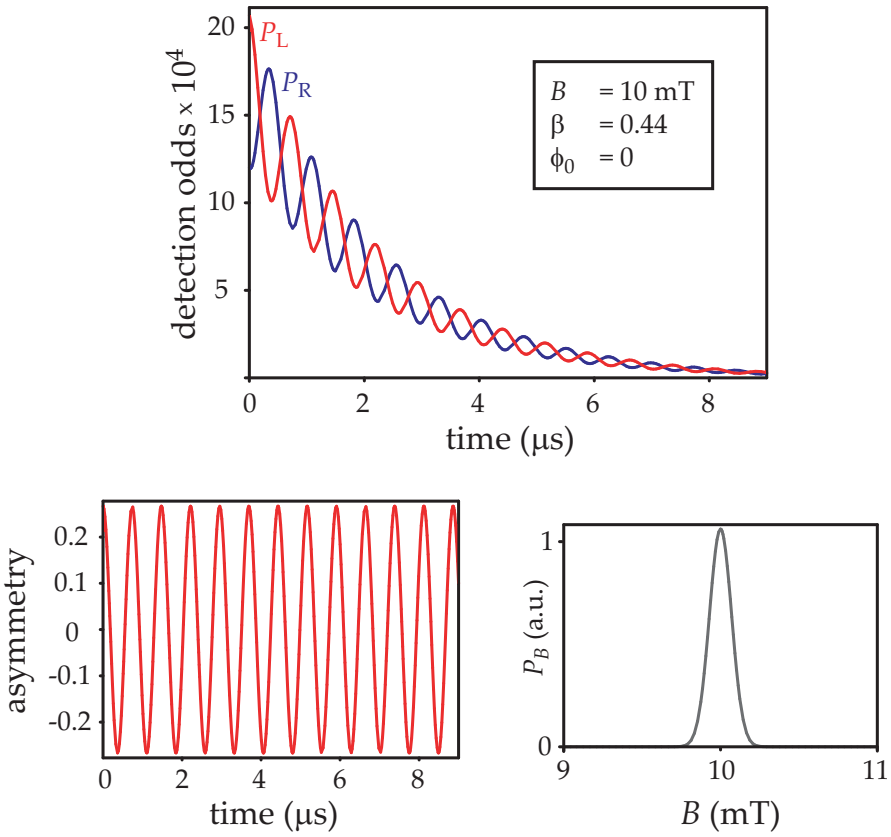

Figure 6.3: The model detector signals P_L and P_R, the asymmetry between them A_0, and the Fourier transform of the asymmetry which gives the distribution of the field

.

in Fig. 6.3 for parameter values as given in the plot. Also shown is that by making a Fourier transform of the asymmetry signal, the muon frequency (or frequencies in general) is (are) recovered and appear as peaks in the spectral plot. This is a way to find out which dominating frequencies (and thus local magnetic field strengths) are present in the sample. In practice, the more advanced "maximum entropy based spectral analysis" (maxent) is used to recover this frequency spectrum. In the real experiment, the muon is implanted into the sample and is not located at a precisely known position. Instead, it has a probability to be at a certain position which depends on the muon energy. These probability profiles can be calculated. So, not only do we need

multiple measurements to collect data from muons which decayed at different times (to follow the spin rotation), we also need a large number of measurements to probe the full spatial distribution of the implanted muons. A typical order of events to count is 10^6 and curves similar to the model signals are then obtained in the form of histograms originating from the counted events at the positron counter detectors. An important difference with the real experiment is that the muons/experiment are/is subjected to decoherence, which results in a damping of the asymmetry signal. Although the frequency spectrum of the asymmetry signal gives important information about the dominating frequencies (local magnetic fields), it does not tell from which part of the sample they originate. The spatial information is lost! Reconstructing the spatial distribution of the magnetic moments inside the sample from the raw data is thus not possible, and the game to play is: assume a certain distribution, calculate the corresponding frequency spectrum (or asymmetry signal), and test how well this fits the measured data.

6.2.2 Experimental setup

At PSI, the muons for the experiment are generated in a secured area and are then directed to the different measurement setups via the main muon transport line. A schematic of the experimental setup is shown in Fig. 6.4, where the entrance point of the muons to the setup is the moderator chamber. The muon transport line and the connecting lines/chambers are all pumped down to a pressure of about 10^{-7} to 10^{-8} mbar.

Generation of the muons

Muons (μ) are unstable elementary particles, decaying in vacuum with a lifetime of 2.2 μs. They are spin-1/2 particles and are positively or negatively charged, with an elementary charge of e. Effectively, the negative muon is like a heavy electron with a mass about 207 times larger, while the positive muon is like a light proton with a mass about 9 times smaller (both types are unstable though). They can be observed in cosmic rays with typical energies in the GeV to TeV range at a (very low) rate of about 100 muons penetrating a square meter every second at sea level. The muon originates from the decay of pions (π), which in accelerators can be produced by bombarding a light nuclear target with high energy protons. Charged pions decay into a muon and neutrino (ν):

$$\begin{aligned} \pi^+ &\rightarrow \mu^+ + \nu_\mu \\ \pi^- &\rightarrow \mu^- + \overline{\nu}_\mu \end{aligned} \tag{6.4}$$

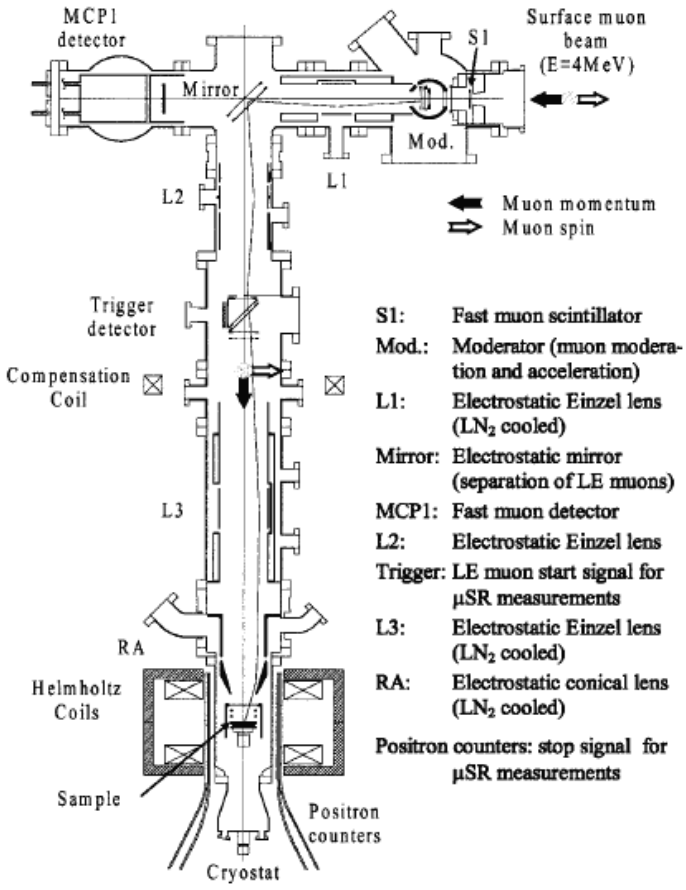

Figure 6.4: The measurement setup area/unit, taken from [73]. Starting from the entrance point for the muon beam, it shows the moderation chamber, the mirror, the trigger chamber and sample chamber, all connected by electrostatic lenses to direct and focus the muon beam.

Due to conservation laws, the produced positive muon (μ^+) has its spin antiparallel to its momentum, while for the negative muon (μ^-) they are parallel. It is possible to create a nearly monochromatic beam of nearly 100 % spin polarized positive muons by selecting the so-called surface muons. These muons are produced by positively charged pions that lost all their energy during the proton bombarding processes and decayed at rest near the surface. The reason that those muons form a near monochromatic beam is that they all have a unique energy of 4.1 MeV and a momentum of 29.79 MeV/c. This process is not possible for the negative muon because the produced π^- particles are

captured much faster inside the target material. Such a monochromatic beam of positively charged, spin polarized surface muons is directed to the measurement area where the muons are implanted into a sample to perform the actual measurement. The energy of 4.1 MeV of these surface muons is sufficiently low for measuring bulk samples, but the stopping profile (the implantation depth distribution) is far too broad (about 0.1 to 1 mm) to investigate thin films. For that, the energy needs to be lowered down to the keV range.

Moderating the muon energy

In the measurement area the incoming surface muons first arrive in the moderator chamber, where a fraction of the muons become trapped into the moderation shield. This shield is a thin layer of a condensed Van der Waals gas (typically argon, neon or N_2 cryosolids) deposited on a much thicker Aluminum foil (about 100 μm thick). In our experiment we used a Ar/N_2 shield with thicknesses of 10 nm and 1.2 nm respectively, at a temperature of 10 K which is necessary for the stability of the shield. The purpose of this shield is to lower the energy of the trapped surface muons down to about 10 eV. The energy lowering mainly takes place in the (relative thick) Aluminum foil, while the deposited Ar/N_2 layer creates a minimum threshold value for the energy of the outgoing muons because of its insulating nature, with a bandgap of 10 to 20 eV. Afterwards they get accelerated again and reach an energy up to about 15 keV. The muon beam (which now consists of surface muons and low energy muons) then gets focussed by an electrostatic Einzel lens onto an electrostatic mirror. This mirror separates the low energy muons (about 15 keV) from the surface muons (about 4 MeV), since it only reflects muons with energies up to few 10s of keV. Muons with higher energies pass straight through it, and are absorbed by the fast muon MCP1 detector. The mirror reflects the momentum, but not the spin of the muon, which remains pointing into the initial direction.

The trigger chamber

The now monochromatic beam of low energy, positively charged, spin polarized muons is focussed by a second electrostatic Einzel lens onto the trigger detector. This detector contains a thin carbon web which emits some electrons whenever a muon passes through and such trigger signals the start of a (new) single measurement. This measurement is completed when a positron counter detector (surrounding the sample space) counts the positron which is emitted by the muon when it decays. The rate at which muons pass through the trigger detector was about 750 per second during our experiments, which gives an

approximate average time window of 1 ms between subsequent passing muons. This is much larger than the muon life time (2.2 μs) so in most cases the single measurement is complete before a new incoming muon is detected in the trigger chamber. The waiting for the positron detection is actually aborted if either a second muon passes the trigger detector or a time window of about 12.5 μs has passed, and the event is discarded.

The sample chamber

To focus the muons onto the sample, a final electrostatic Einzel lens is used. The sample itself is mounted such that it is electrically insulated and can be set to a high voltage (up to $\pm$12 kV) in order to accelerate or decelerate the muons before implantation. In this way the energy of the muons can be fine-tuned and the appropriate stopping profile can be selected. Fig. 6.5 shows the stopping profile for the actual sample we measured, which was a Si/Py(50)/Nb(50)/Py(20)/Nb(2) thin film, where numbers represent the layer thickness in nm. The depth is measured starting from the top surface of Nb(2) layer, meaning that the center of the Nb layer is at a depth of 47 nm. As can be seen, a muon energy of 5 keV has the main peak just inside the Nb and thus focusses on the interface region. Increasing the muon energy shifts and broadens this main peak, such that for energies of 10 keV to 15 keV the full Nb layer is probed, with a focus near the central part of the layer. The muon energy thus takes the role of the spatial coordinate directed normal to the surface, and ideally, the magnetic moments in the sample only vary along this normal direction. The experiment is performed in the presence of an applied magnetic field which is homogeneous across the sample space and parallel to the sample plane. Fig. 6.6 shows a top-view of the sample space where the incoming muon μ^+ arrives from the left side (with momentum p and spin s). The magnetic field bends the muon flight path through the Lorentz force it exerts on them. This is compensated for by the transverse electrical field E set by the high voltage potentials RAL and RAR. These voltages needs to be fine-tuned such that the spot of the muon beam is at the center of the sample and not towards one of the two positron detectors. In practice the spot is always slightly more on one of the two sides such that the detector on that side detects more then the other detector. This affects the asymmetry but that can be corrected for (in the limit of small displacement error) by multiplying one of the two counter detector signals to re-balance this difference. For our experiments, this adjusting parameter α for the left counter detector was about 0.99, indicating a fairly good alignment of the muon beam. For the applied magnetic field we used 10 mT directed along the vertical. This field sets a base frequency of $f = 1.35$ MHz for the muon precession which comes down

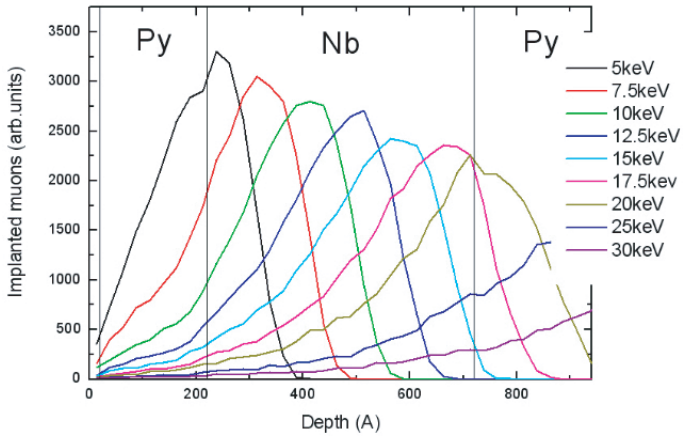

Figure 6.5: Calculated muon stopping profile for a Nb(2)/Py(20)/Nb(50)/Py(50) layered sample (numbers representing the layer thickness in nanometer) for different implantation energies. The depth = 0 is at the top surface of the Nb(2) layer.

to almost 3 rotations per τ_μ, making it a reasonable base frequency to follow.

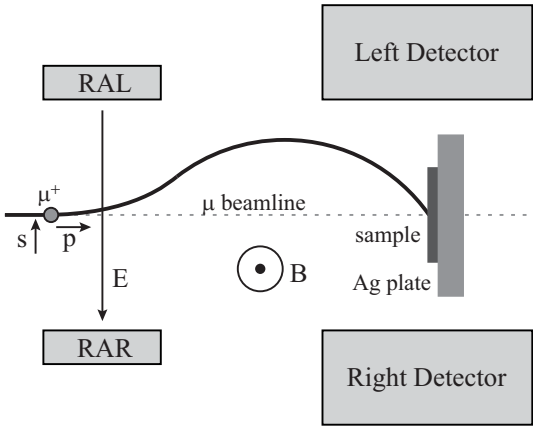

Figure 6.6: Top-view schematic of the sample space showing the muon path of flight, which is centered onto the sample by the electrical field E and induced magnetic field B. RAL and RAR are high voltage potentials creating E.

Implanting a muon

The muon is now adjusted for implantation energy and focussed at the sample center. It penetrates the sample (or the Ag backing plate, because the spot is slightly larger than the sample itself) and comes to rest at time t_0, measured with respect to the moment it passed the trigger chamber. Subsequently, it starts precessing around the local field it experiences until the moment it decays into a positron (and a muon antineutrino and electron neutrino). The measurement stops when this positron is detected by any of the positron counter detectors (which are outside the UHV area). The direction in which the positron is emitted is preferentially along the momentary spin direction of the muon, but its distribution is energy dependent with the energy-averaged form given by Eq. 6.2. Due to the near monochromatic near 100 % polarized muon beam, the initial spin and momentum state of all incoming muons are practically identical, and all the single measurements (events) are thus coherent and can be added. Typically several million of events are necessary to obtain high enough statistics for further data analysis (i.e. for each depth to be probed by enough muons to cover the spread in the positron emission angle). The primary sources of decoherence of the muons are fluctuations in the local field (changes to the sample) and the momentum spread of the beam itself (changes to the muon), which is supposed to be some 10s of eV. The field fluctuations disturb the precession frequency itself which directly leads to decoherence if it is significant compared to the local (average) value. A direct implication of the momentum spread of the beam is a spread in the time-of-flight, resulting in a spread of some 10s of nanoseconds in the time t_0. The result is a sharp non-exponential decay of detector signal during the first to 20 to 30 ns after t_0. Therefore, data collected during these early times are left out of the data analysis. The time resolution of the detection system is close to 200 ps, which is the used size for the time bins. A valid positron count adds 1 count to the time bin which contains the relative time of decay (relative to the moment the muon was detected in the trigger detector). To give an idea of the histogram filling, a time span of 2.2 μs (the muon life time) is divided in 11000 time bins of 200 ps, and the full time window of the measurement contains about 66000 time bins. Collecting 10^7 events (our typical measurement statistics) then gives an average filling of about 75 events per time bin per detector, which means about 450 events in the early time bins of the detector (when taking an exponential decay with a characteristic time of 2.2 μs).

6.3 Results

6.3.1 Experimental details

The sample used for the LE-μSR measurements is a Py(50)/Nb(50)/Py(20) trilayer thin film, with the numbers representing the layer thickness in nm. To cover a large fraction of the sample plate, 16 pieces of 1×1 cm^2 were put together forming a 4×4 cm^2 mosaic (see Fig. 6.7). All pieces were made under identical conditions, with the same deposition parameters as for the Py/Nb/Py spin-valve devices (see Ch. 5). The pieces are glued to the sample plate with conducting Ag-paste, all with the orientation of the easy axis aligned with the applied field during the measurement. This conducting Ag-paste is also used to electrically connect the top layers of the individual samples to ground them to the sample plate (such that the final implantation energy of the muons can be tweaked by setting a high potential). With this covering, it is expected

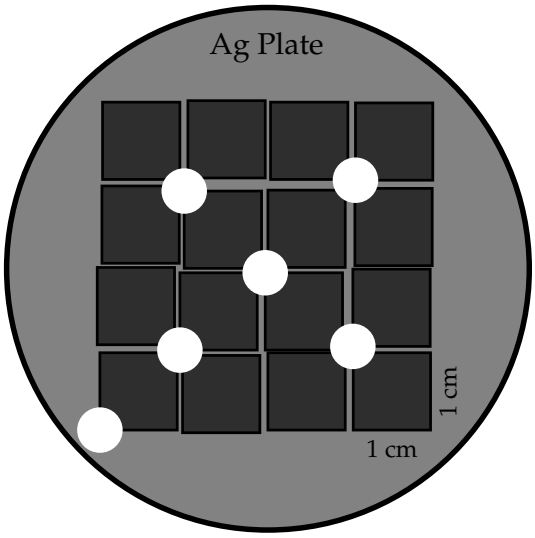

Figure 6.7: Sketch of the sample pieces forming a 4×4 mosaic, glued on the round sample plate. White dots represent the conducting Ag-paste, electrically connecting all pieces to the sample plate.

that around 90 % of the incoming muons will hit the sample [76]. The rest of the muons gets implanted into the Ag backing plate, where only the external field is probed. The sample plate is mounted into the sample chamber with its surface perpendicular to the incoming muon beam. The sample pieces are oriented such that the easy axis of the Py is aligned along the setup vertical, which is parallel to the external field direction, which is significantly

higher than the coercive fields of the thin Py films, which are close to 0 mT. During the experiment the applied field was 10 mT directed from bottom to top. The corresponding muon precession frequency is 1.35 MHz with a anticlockwise rotation direction when looking from above. The rotation plane is perpendicular to the field direction and the initial spin direction points towards the left counter detector (see Fig. 6.6). Measurements were performed at two different temperatures, either at $T = 10$ K (Nb in normal state) or $T = 4.5$ K (Nb in superconducting state). For each temperature, the sample is probed at eight different muon implantation energies, $E_{\mathrm{muon}} = 5$, 5.5, 6, 6.5, 7, 7.5, 10 and 12 keV. The lowest muon energy has its stopping distribution focussed near the S/F interface, while the highest two covers the full sample, with a focussed near the center of the Nb layer. Furthermore, for $T = 4.5$ K we did the measurements for both a "field cooled (FC)" and "zero field cooled (ZFC)" treatment. For FC the applied field was kept on during cooldown from normal state to superconducting state, for ZFC the fields was switched off during cooldown. In total we thus have 24 data sets, where for each data set we collected 10^7 counts (positron detections). In terms of pure measurement time these 10^7 counts comes down to almost 4 hours of measuring (at a rate of 750 incoming muons per second).

6.3.2 Fitting of the data

To obtain information about the magnetic profile we attempt to fit the measured detector signals (the real-time raw data) rather than analyzing the Fourier transform of the asymmetry data (the frequency spectrum). An example of a maxent analysis (Fourier transform of the asymmetry signal) is given in Fig. 6.8, where the data is from a muon energy of 5 keV with $T = 10$ K. As is clear from the graph, no outstanding features appear other than the main peak which is centered at a field of 9.79 mT. This is the main reason why we focussed our data analysis on the real-time data. The strategy we applied starts by making a best fit to the raw detector data using the Levenberg-Marquardt alogrithm [77]. Including the spatial dependence of the magnetic profile is not possible (each location should then be parameterized by an unknown precession frequency), instead a simple uniform profile is used.

The fit functions

The detector signals as derived before (Eq. 6.3) give the fractional chance of counting the positron at time t. This is for a single muon at a fixed position. When adding these contributions from many (coherent) muons we have to correct for decoherence (or dephasing). Taking a (standard) exponen-

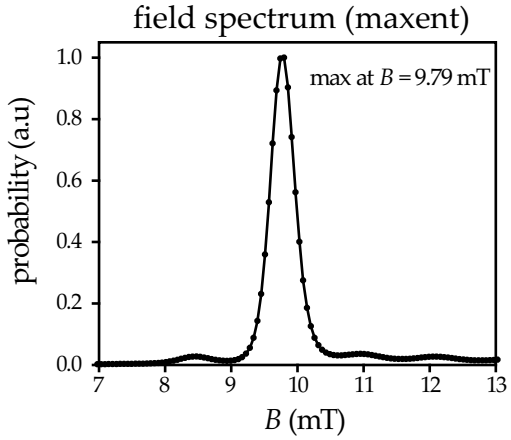

Figure 6.8: Probability distribution of the local fields in the Nb layer, for the data set with muon energy of 5 keV and temperature of 10 K. Results are obtain using a maximum entropy (maxent) analysis.

tial dephasing for the asymmetry with a characteristic time τ_θ, the fractional counting probabilities become:

$$P_{\mathrm{R,L}}(t) = \frac{\beta'}{\tau_\mu}\left(1 \mp A_0(t)\, e^{-\frac{t}{\tau_\theta}}\right) e^{-\frac{t}{\tau_\mu}} \tag{6.5}$$

Furthermore, the incoming muon is implanted in one of the following 3 areas: 1) the Ag backing plate, 2) the Nb layer, or 3) the Py layer. Although we cannot include a full spatial dependence into the fitting, it is rather straightforward to distinguish between these three areas, all characterized by a single average field B_i, with i being the label of the area. These areas then all have a different asymmetry function A_0^i and a fractional chance for the muon to stop in that area of P_i, with $P_\mathrm{Ag} + P_\mathrm{Nb} + P_\mathrm{Py} = 1$. The muons implanted in the Ag backing plate and the Nb layer all experience a field equal to, or close to the applied field and are expected to experience a very similar dephasing. However, in the Py the internal field is orders of magnitude larger then the applied field. In fact, it is far above the maximum detectable frequency of 50-70 kHz of the LE-μSR setup, and thus can be treated as instantly dephased ($\tau_\theta \to 0$). Adding this the fractional chances become:

$$P_{\mathrm{R,L}}(t) = \frac{\beta'}{\tau_\mu}\left(1 \mp \left(P_\mathrm{Ag} A_0^\mathrm{Ag}(t) + P_\mathrm{Nb} A_0^\mathrm{Nb}(t)\right) e^{-\frac{t}{\tau_\theta}}\right) e^{-\frac{t}{\tau_\mu}} \tag{6.6}$$

In the correct case, the detector detect the positrons coming from the decay of the muon under investigation. However, this signal is polluted by anomalies

(like scattered positrons). This we model by adding a (small) time independent probability of such fake events which turns out to work very well. The final fit equations, the number of counted events as function of time, are obtained by simply multiplying by the fractional numbers by a general amplitude N_0 (which is not exactly equal to the total number of counted event due to renormalization).

$$\begin{aligned} N_{\mathrm{R}}(t) &= N_0\beta'\left(1-\left(P_{\mathrm{Ag}}A_0^{\mathrm{Ag}}(t)+P_{\mathrm{Nb}}A_0^{\mathrm{Nb}}(t)\right)e^{-\frac{t}{\tau_\theta}}\right)e^{-\frac{t}{\tau_\mu}}+N_{\mathrm{f,R}} \\ N_{\mathrm{L}}(t) &= \tfrac{1}{\alpha}N_0\beta'\left(1+\left(P_{\mathrm{Ag}}A_0^{\mathrm{Ag}}(t)+P_{\mathrm{Nb}}A_0^{\mathrm{Nb}}(t)\right)e^{-\frac{t}{\tau_\theta}}\right)e^{-\frac{t}{\tau_\mu}}+N_{\mathrm{f,L}} \\ A_0^{\mathrm{i}} &= -\tfrac{1}{6\pi\beta'}\left(\sin\left(\phi(t)-\pi\beta'\right)-\sin\left(\phi(t)+\pi\beta'\right)\right) \\ \phi(t) &= \gamma_\mu B_{\mathrm{i}}t+\phi_0 \end{aligned} \tag{6.7}$$

Here $N_{\mathrm{f,R}}$ and $N_{\mathrm{f,L}}$ account for the pollution, and we incorporated the setup alignment factor α to correct for the misalignment of the muon spot (see text related to Fig. 6.6). When we subtract the linear offsets $N_{\mathrm{f,R}}$ and $N_{\mathrm{f,L}}$, the asymmetry signal becomes very simple:

$$A(t)=\frac{\alpha N_{\mathrm{L}}(t)-N_{\mathrm{R}}(t)}{\alpha N_{\mathrm{L}}(t)+N_{\mathrm{R}}(t)}=\left(P_{\mathrm{Ag}}A_0^{\mathrm{Ag}}(t)+P_{\mathrm{Nb}}A_0^{\mathrm{Nb}}(t)\right)e^{-\frac{t}{\tau_\theta}} \tag{6.8}$$

Details of the fitting

The parameters to fit can be divided into the following groups: (i) P_{Ag}, β', τ_θ, α, the setup/system constants; (ii) B_{Nb}, P_{Nb}, ϕ_0, the implantation energy (and system temperature) dependent parameters; and (iii) N_0, $N_{\mathrm{f,L}}$, $N_{\mathrm{f,R}}$, the amplitudes of the signal. The parameter $\tau_\mu = 2.197$ μs is a natural constant with a well determined value and for the applied field we use $B_{\mathrm{Ag}} = 9.79$ mT, which we found was the actual value of the applied field (see Fig. 6.8, which is taken at low muon energy where the contribution of the background is dominant over the sample contribution). The main strategy we follow is to first determine the fit parameters of group (i) by stacking all data sets (to improve the accuracy) and next to fix those values and fit the individual data sets to determine the parameters of group (ii) as function of the implantation energy. By fitting the stacked data, we also obtain values for the parameters of group (ii); however, these values represent some average value for the different implantation depth. The parameters of group (iii), although not depending on the implantation energy, also have to be determined for each individual data set because they directly depend on the number of counts, and this number is close to 10^7, but not exactly the same for all sets.

Before fitting we re-bin the original time bins with a factor of 32, such that now each bin is approximately 6.4 ns. This we mainly do to smooth the raw data. Furthermore, we adopted the convention for the fit functions to set the time at the starting of the precession (t_0) to zero. However, this time is not precisely known and neither is it the same for different implantation energies. This (small) time deviation leads to a small difference in the starting angle ϕ_0, which thus must be a free parameter during the fitting. For all fits, we use the $t = 650$ ns after triggering as the t_0 time, while we start the fitting at $t = 750$ ns. All presented data have the time such that $t = 0$ is at the moment of the trigger detection. The fitting follows an iterative process which minimizes the sum of the squared errors according to the Levenberg-Marquardt algorithm. Let $y(x_i)$ be the measured data at discrete points x_i, with an experimental error that can be approximated by a Gaussian distribution with standard deviation σ_i. If the fit to this data is given by $y_{\text{fit}}(x_i)$, then the statistical (total) error of the fit is given by $\text{Err} = \chi^2/x_N$, with x_N the number of points to fit, and χ^2 defined by:

$$\chi^2 = \sum_i \left(y_{\text{fit}}(x_i) - y(x_i)\right)^2 / {\sigma_i}^2 \tag{6.9}$$

With this definition of the total error, a value close to 1 means in general a good fit. This is because in that case, the difference between the fit and the real data is on average within the error of the experimental data itself.

Fitting the stacked data

Fig. 6.9 shows the fit result of the stacked detector data. Blue and red dots are the measured right and left detector signals respectively and the fits to them are the solid black lines. The inset shows a zoom-in of a part of the main plot (numerical values along the axis are in the same units as the main plot). Also shown in the inset are the values obtained of the fit parameters of group (i) and the errors of the fits. The values of the parameter of group (ii) are not shown here, instead they are slightly more accurately determined in a next fitting shown in the Fig. 6.10. In general, all obtained values are very reasonable and the quality of the fit is good. At $t = 0$ the muon is detected and the initial flat part is the time it takes for the muon to get implanted. The contribution to the signal coming from the Ag backing plate $P_{\text{Ag}} = 20.2$ % is a bit more than the expected 10 %, which is likely due to our pieces not closing perfectly and having several big silver-paste drops on top for the grounding. The value of β implies an effective angular covering of about 70 %, the dephasing time is close to 1 μs, which is equivalent to about 1.4 periods of a muon in the applied field. A value of 0.988 for the correction parameter α means a well-centered

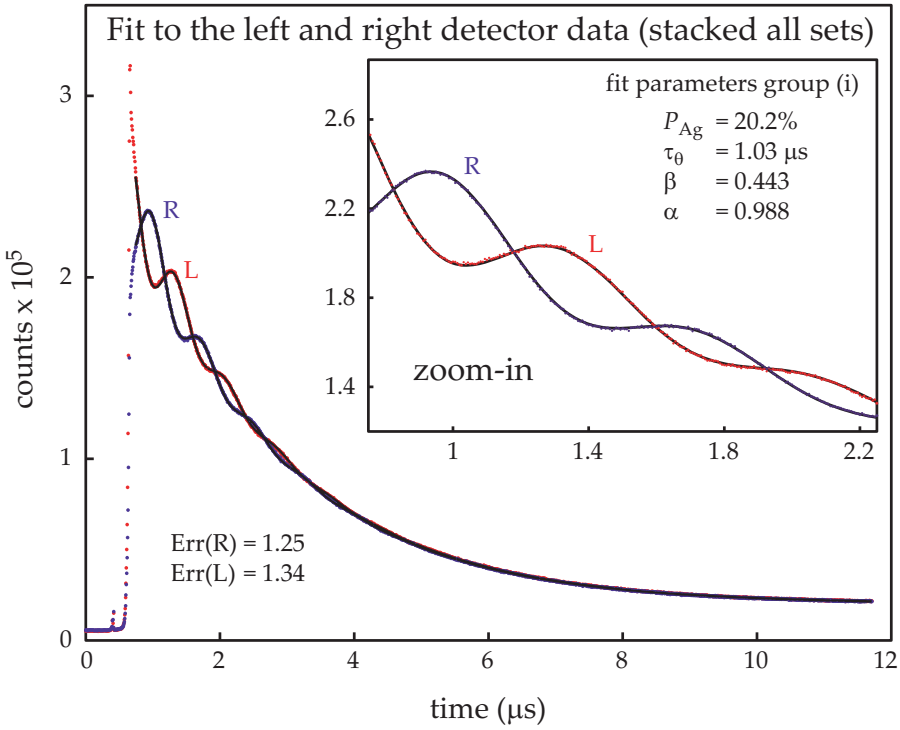

Figure 6.9: Best fit for the stacked detector signals. Blue/red dots are the measured right/left detector data, with the solid black lines the obtained best fits with errors Err(R)/Err(L). The inset is a zoom-in and also shows the values of (part of) the fit parameters (the ones independent on the muon implantation energy).

beam (about 1 % misalignment). These parameter values are from here on fixed for all further fitting.

From the left and right detector signals the asymmetry signal is constructed (see Eq. 6.8) and the fit results are given in Fig. 6.10, where an additional linear offset is included to easy the fitting to correct for the remaining misalignment. The red dots are the asymmetry signal with the fit given by the solid black line. The values obtained for the fit parameters are given in the plot and the most interesting one is B_{Nb} which apparently (on average) is *lower* than the background field of 9.79 mT. An additional comparison fit (grey line) is made with fixed $B_{\mathrm{Nb}} = B_{\mathrm{Ag}} = 9.79$ mT. Although the visible change is small, the error of the fit has drastically worsened. The value for P_{Nb} seems very reasonable comparing to the muon implantation profile and the value for ϕ_0 corresponds to a starting angle of about 21° (which would take a muon pre-

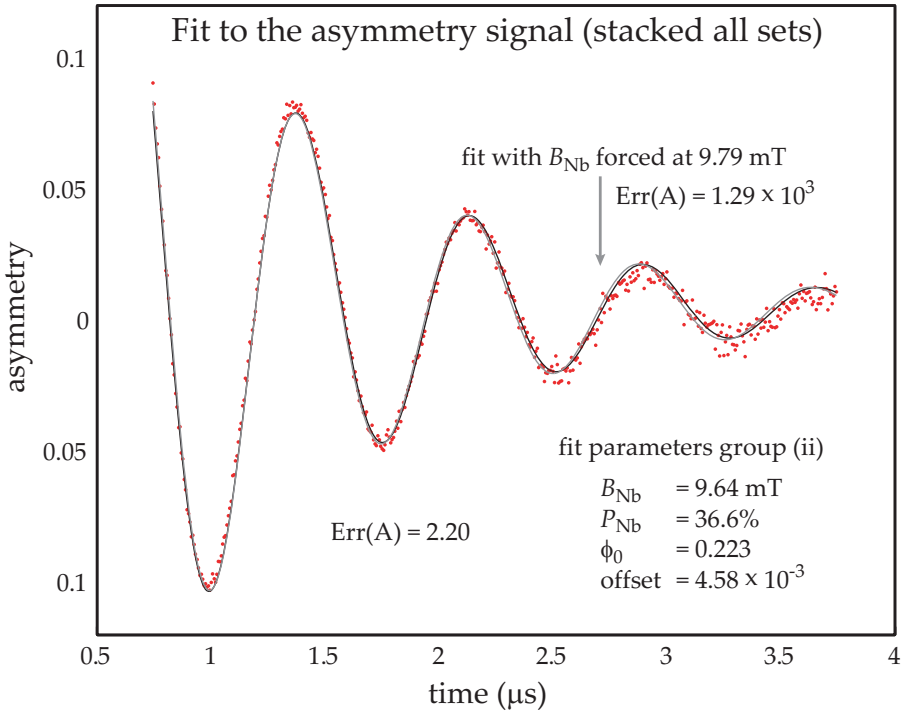

Figure 6.10: Asymmetry signal of Fig. 6.9. The solid black line is the best fit with error and parameter values as given in the plot. A second fit (grey line) is made with $B_{\mathrm{Nb}} = B_{\mathrm{Ag}}$ from which only the error is given.

cessing in the applied field about 40 ns). These extracted values are *averages* and we will make fits to the single data sets to obtain the muon-energy dependence of these parameters, which correlates to the spatial dependence of the parameters. In total, from the stacked fittings we have obtained:

setup constants	
P_{Ar}	$= 20.2$ %
τ_θ	$= 1.03$ μs
β	$= 0.443$ rad
α	$= 0.988$

parameters to fit (obtained averages)	
$\langle P_{\mathrm{Nb}} \rangle$	$= 36.6$ %
$\langle B_{\mathrm{Nb}} \rangle$	$= 9.64$ mT
$\langle \phi_0 \rangle$	$= 0.223$ rad

Fitting the individual data sets

For each individual data set, fits are made to the asymmetry signals. For muon energies of 5 keV and 10 keV, these fits are shown in Fig. 6.11, where from top to bottom we have the $T = 4.5$ K (ZFC), $T = 4.5$ K (FC) and $T = 10$ K

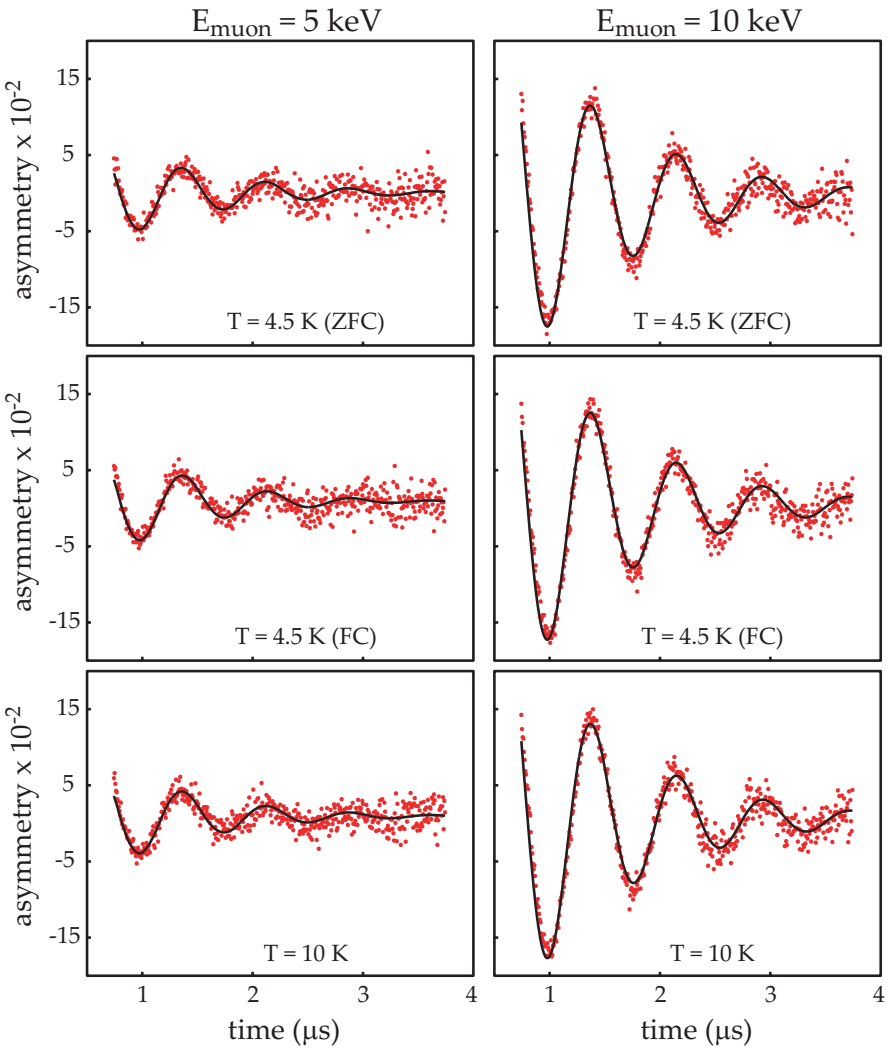

Figure 6.11: Fits to the asymmetry data with muon energies of 5 and 10 keV, taken at temperatures of 10 K and (2x) 4.5 K, one with field cooled (FC) conditions and one with zero field cooled (ZFC) conditions.

data sets. The results obtained for the parameters P_{Nb} and B_{Nb} are shown in Fig. 6.12 and for ϕ_0 and the total error in Fig. 6.13, all as function of the muon energy. For all graphs the green lines are from the data at $T = 10$ K. The red and blue lines are from the data at $T = 4.5$ K, with red for the FC treatment and blue for the ZFC treatment. The results for P_{Nb} are in accordance with

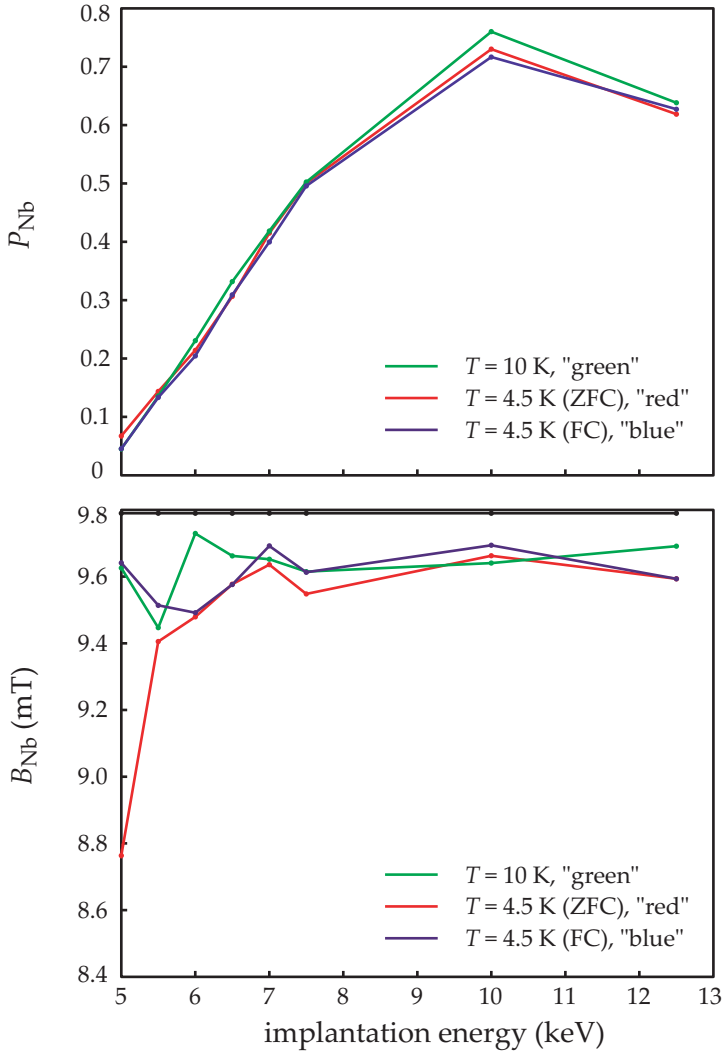

Figure 6.12: Fit parameters P_{Nb} and B_{Nb} as function of the implantation energy of the muons, with green: $T = 10$ K, red: $T = 4.5$ K (field cooled) and blue: $T = 4.5$ K (zero field cooled). Also shown is the value of the applied field of 9.79 mT

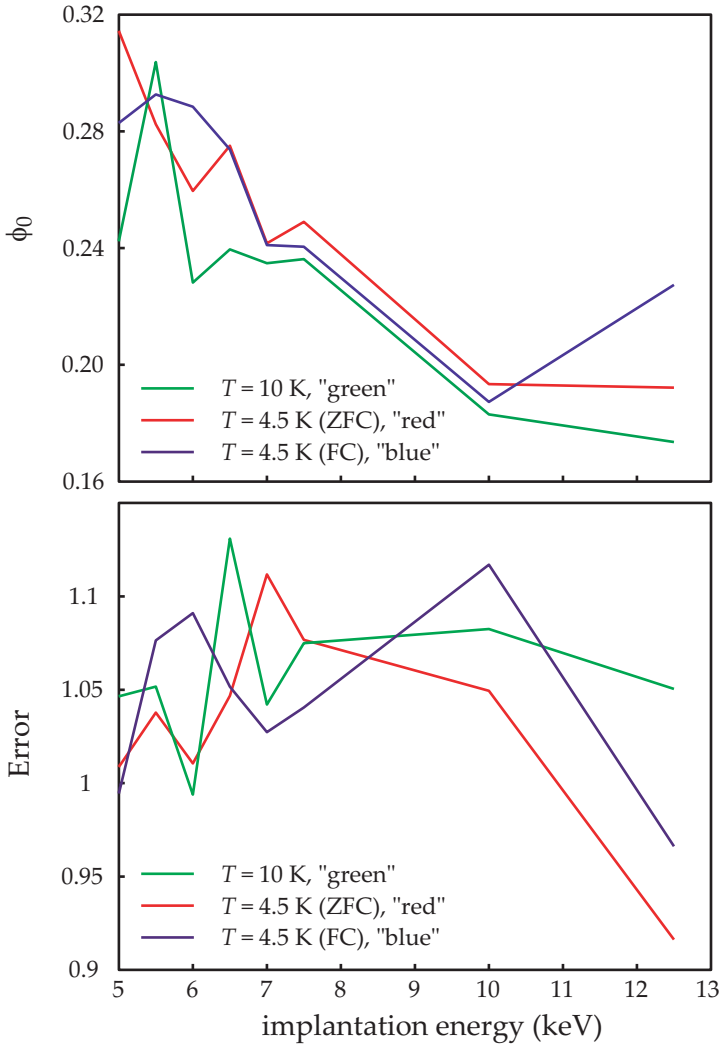

Figure 6.13: Fit parameter ϕ_0 and the error as function of the implantation energy of the muons, with green: $T = 10$ K, red: $T = 4.5$ K (field cooled) and blue: $T = 4.5$ K (zero field cooled).

the stopping profile showing a decrease for lower implantation energies. Also, the three separate curves don't vary much from one to another. The results for B_{Nb} are the most interesting ones because it contains information about the field profile which we try to unravel. It shows that the green (10 K data) and blue (ZFC data) curve are about the same, while the red one (FC data) comes down at the lowest energy. We believe that this decrease to a significantly lower local field value observed for the lowest implantation energy (= closest to the interface) is a signature of the reverse proximity effect. However, we are left with several questions. Why do the ZFC data not show this lowering, why are the all lines significantly below the background field of 9.79 mT, and why do normal state data not really differ from the data taken in the superconducting state.

6.3.3 Discussion and conclusion

To start the discussion with the $T > T_c$ data, it can be surmised that the (global) stray fields coming from the F layers will curl into the Nb layer where they are now directed anti-parallel to the applied field. They exit the Nb layer at the opposing side and curl back into the F layer. This leads to a lowering of the field in the Nb layer. Making a model calculation of the induced field B coming from a homogeneously magnetized squared plate with surface area $L \times L$ and thickness $d \ll L$, we find that at a distance $x_0 \ll L$ away from the surface center (along the surface normal) B approximately is given by:

$$B\left(x_0\right) \sim \tfrac{\mu_0 m_0}{\pi}\left(\arctan\left(\tfrac{x_0}{\sqrt{2}L}\right) - \arctan\left(\tfrac{x_0+d}{\sqrt{2}L}\right)\right) \sim -\tfrac{\mu_0 m_0}{\pi}\tfrac{d}{\sqrt{2}L} \qquad (6.10)$$

where m_0 is the density of magnetic moments inside the plate (in units of A/m) and $\mu_0 = 4\pi\ 10^{-7}$ N/A^2 the magnetic constant. The result is independent of x_0 and the minus sign means a direction opposite to the magnetic moments in the F layer. Consequently, in our F/S/F devices we can expect a global lowering of the field inside the Nb layer. However, inserting the numbers $L = 1$ cm, $d = 70$ nm and $m_0 = 0.834 \times 10^6$ A/m (using an atom density of $0.899\ 10^{29}$ m^{-3} and an average moment per atom of $1.1\mu_B$), gives a value of $\sim 1.8\ \mu$T, which is significantly less than what we observed. For the $T < T_c$, both the FC and ZFC data are not significantly different from the normal state data for the higher energies. This indicates that no Meissner screening is taking place in the superconducting state. Furthermore, in the ZFC case, the magnetization in the F layer is inhomogeneous because the coercive field for such macroscopic sample is very close to zero (of the order of 0.1 mT). A complex domain state will appear with stray fields connecting the two F layers

across the Nb layer. When such state is frozen during the cool down, it brings vortices crossing the Nb layer, which might in turn pin the domain state in the F layers. Essentially we now have created inhomogeneous magnetization at the interface. This will *reduce* the polarization of the Cooper pairs and is in line with the disappearance of the dip in the fit results. It stands to reason therefore that only the FC state creates the circumstances in which the inverse effect is to be found, and then only for the lowest implantation energies. If there is any effect to see, it is close to the limit of the accuracy of the measurements. Furthermore, it is only for the lowest implantation energy that we are probing close enough to the interface to detect a possible inversion effect. On the other hand, a consistent picture starts to form. In recent works, by different measurement techniques, indications for the existence of the reverse proximity effect have been observed as well [71, 72]. To claim any real sign of the "polarization of the Cooper pairs", more data analysis is needed, where special attention should be paid to the surface roughness of the interface, which smears out the effect due to lateral inhomogeneity in the local fields.